JPhys Energy

PAPER • OPEN ACCESS

Stabilization of Ce^{3+} cations via U–Ce charge transfer in mixed oxides: consequences on the thermochemical water splitting to hydrogen

To cite this article: Carlos Morales *et al* 2025 *J. Phys. Energy* **7** 025012

Journal of Physics: Energy

PAPER

Stabilization of Ce^{3+} cations via U–Ce charge transfer in mixed oxides: consequences on the thermochemical water splitting to hydrogen

Carlos Morales[1], **Rudi Tschammer**[1], **Thomas Gouder**[2], **YongMan Choi**[3], **Dalaver Anjum**[4], **Aman Baunthiyal**[5], **Jon-Olaf Krisponeit**[5,6], **Jens Falta**[5,6], **Jan Ingo Flege**[1,*] and **Hicham Idriss**[7,8,*]

[1] Applied Physics and Semiconductor Spectroscopy, Brandenburg University of Technology Cottbus–Senftenberg, Konrad-Zuse-Strasse 1, D-03046 Cottbus, Germany
[2] European Commission, Joint Research Centre (JRC), Postfach 2340, D-76125 Karlsruhe, Germany
[3] College of Photonics, National Yang Ming Chiao Tung University, Tainan 71150, Taiwan
[4] Department of Physics, Khalifa University, Abu Dhabi, United Arab Emirates
[5] Institute of Solid State Physics, University of Bremen, 28359 Bremen, Germany
[6] MAPEX Center for Materials and Processes, University of Bremen, 28359 Bremen, Germany
[7] Institute of Functional Interfaces (IFG), Karlsruhe Institute of Technology (KIT), 76344 Eggenstein-Leopoldshafen, Germany
[8] Department of Chemistry, University College London, UCL, London WC1E 6BT, United Kingdom
* Authors to whom any correspondence should be addressed.

E-mail: JanIngo.Flege@b-tu.de, hicham.idriss@kit.edu and h.idriss@ucl.ac.uk

Keywords: mixed oxide $Ce_{1-x}H_xO_2$, thermochemical water splitting (TCWS) reaction to hydrogen, XPS U4f, XPS Ce3d, Ce^{4+} reduction to Ce^{3+}, U^{4+} oxidation to U^{5+} and U^{6+}, DFT + U computation of oxygen vacancies

Supplementary material for this article is available online

OPEN ACCESS

RECEIVED
8 January 2025

REVISED
20 February 2025

ACCEPTED FOR PUBLICATION
26 February 2025

PUBLISHED
7 March 2025

Abstract

The work's objective is to enhance the generation of H_2 via the thermochemical water splitting (TCWS) reaction over nanocrystalline mixed oxide $Ce_{1-x}U_xO_2$. While CeO_2 is the most active and stable known reducible oxide for the TCWS reaction, it is below par to make it practical. This has motivated many works to enhance its reduction capacity and therefore increase its activity. In this work the presence of both metal cations (Ce^{4+} and U^{4+}) has allowed for the charge transfer reaction to occur ($Ce^{4+} + U^{4+} \rightarrow Ce^{3+} + U^{5+}$) and therefore increased its capacity to generate oxygen vacancies, V_O ($2\,Ce^{3+} + V_O$), needed for the TCWS reaction. Test reactions on the polycrystalline mixed oxides indicated that small atomic percentages of U (<10%) were found to be optimal for H_2 production (ca. 7 μmol g^{-1}) due to a considerable increase of Ce^{3+} states. Further studies of the Ce–U interaction were performed on thin epitaxial $Ce_{1-x}U_xO_2$ (111) films of about 6 nm. *In situ* x-ray photoelectron spectroscopy showed clear evidences of charge transfer at low U content (ca. 50% of surface/near surface Ce^{4+} cations were reduced in the case of $Ce_{0.95}U_{0.05}O_{2-\delta}$). Moreover, it was found that while increasing the content of U decreased the charge transfer efficiency, it protected reduced Ce^{3+} from being oxidized. Our computational results using the DFT + U method gave evidence of charge transfer at 3.5 and 6.2 at.% of U. In agreement with experiments, theoretical calculations also showed that the charge transfer is sensitive to the distribution of U^{4+} around the Ce^{4+} cations, which in turn affected the creation of V_O needed for water splitting. Our results point out to the important yet often neglected effect of statistical entropy (cations distribution in the lattice), in addition to composition, in increasing the density of reduced states and consequently enhancing H_2 production from water.

1. Introduction

The dynamic of the reduction and oxidation of metal oxides affects their properties and, in turn, their performance in many applications such as in catalysis [1], sensors [2], and solar thermal reduction [3, 4] of water to hydrogen or CO_2 to CO. While many oxides such as CuO/Cu_2O, Fe_2O_3/Fe_3O_4, and

TiO_2/TiO_{2-x} ($x < 0.5$) have considerable redox properties [5], cerium oxide (CeO_2/CeO_{2-x}, $x < 0.5$) in particular stands out as one of the most active and stable reducible metal oxides [6]. However, its reduction requires high energy. In catalysis, the reduction of an oxide is traditionally conducted by using a chemical compound (chemical energy), such as molecular hydrogen in methanol synthesis [7] or carbon monoxide in the water gas shift reaction [8]. As the generation of hydrogen and CO by steam methane reforming contributes considerably to CO_2 emission, solar thermal-driven reactions are desired when looking beyond a hydrocarbon-based energy system. In this case, a metal oxide is heated to a high temperature, using concentrated solar light, in an inert environment [9] and then exposed to water or CO_2 to release H_2 or CO as per the following equations:

$$\begin{aligned} MO_X &\rightarrow MO_{x-\delta} + \delta/2\ O_2 && \text{(Step 1)} \quad +\Delta G_r && (1)\\ MO_{x-\delta} + \delta\ H_2O &\rightarrow MO_x + \delta\ H_2 && \text{(Step 2)} \quad -\Delta G_r && (2)\\ +\delta\ CO_2 &\rightarrow MO_x + \delta\ CO && \text{(Step 2}') \quad -\Delta G_r && (2') \end{aligned}$$

where $MO_{x-\delta}$ is a binary oxide, in which x refers to the stoichiometry of the compound and δ represents the deviation from stoichiometry due to reduction, and ΔG_r is the Gibbs free energy of the reaction.

This approach comes with a high cost as temperatures exceeding 1500 K are typically needed to make nonnegligible quantities of lattice oxygen vacancies in cerium oxide (CeO_{2-x}, where x is <0.5) [10], which produce 10 ml H_2/g per cycle in practical conditions when using a solar reactor [3]. Many computational studies have indicated that the energy needed to create an oxygen vacancy in the bulk of CeO_2 is about 3 eV [11–13], whereas the energy required for atomic oxygen diffusion is less than 1 eV [14]. Despite the relatively fast reaction kinetics for the redox cycle, which is highly desired for steps 1 and 2, the high energy cost makes the process unsustainable (at present, estimates of the levelized cost of hydrogen produced by the thermochemical water splitting (TCWS) method is about 10 USD per kg, which is about ten times the present cost from fossil fuels) [15]. CeO_2 has shown excellent stability for redox cycles that extends for years (for example, in its use as a support in three-way catalytic converter catalysts) [1, 6]. However, the TCWS reaction solely relies on the O-defect density, which is, per mass, low in CeO_2. Thus, many approaches have been developed to either find alternative oxides or mix CeO_2 with other metal cations to decrease the reduction energy and consequently increase the reduced state density [16]. Among these strategies are those related to charge transfer. In this case, a fraction of Ce^{4+} cations from the CeO_2 matrix are substituted by another element, resulting in a mixed metal oxide. In that regard, many studies are devoted to the TCWS reaction upon adding metal cations (by substitution, interstitial, or in a mixed phase) to CeO_2. For example, a study focused on Fe, Co, Mn, and Zr (10 mol %) in CeO_2 was conducted, highlighting stability issues despite high first-cycle activity (of the order of a few ml $(H_2)/g_{oxide}$) [17]. Generally, the substitute element must meet a few requirements to do this most efficiently: (i) similar ionic size to Ce^{4+}, (ii) the same crystallographic structure (fluorite) to minimize phase segregation, and (iii) being easily oxidized to higher oxidation states (+5 and/or +6). Among potential candidates, U^{4+} cations in uranium dioxide (UO_2) are the most suitable, if not the only possible cations that fulfill these requirements. In this case, the substitution of a fraction of Ce^{4+} by U^{4+} would result in a charge transfer as in the following equation:

$$Ce^{4+}\left(4f^0\right) + U^{4+}\left(5f^2\right) \rightarrow Ce^{3+}\left(4f^1\right) + U^{5+}\left(5f^1\right). \quad (3)$$

The redox properties of such a system have been experimentally studied by others [18–20] and us in the past [12, 21, 22]. Indeed, experimental evidence of charge transfer was seen, and the results converged on one important point: The optimal efficiency for charge transfer between Ce and U cations occurs at low at.% of U, where the creation of Ce^{3+} cations is maximized. In addition, the activity of this mixed oxide, in its polycrystalline form, toward water splitting to hydrogen was investigated by one of us [21, 22]. In these studies, the mixed oxide $Ce_xU_{1-x}O_{2\pm\delta}$ was reduced by H_2 at 973 K to prevent phase segregation for the hydrogen production and by Ar^+ sputtering for the core level spectroscopy measurements to monitor the charge transfer. These experiments also showed, in line with spectroscopic evidence, that low levels of U substitutions were better for hydrogen production than higher levels, with an experimental optimum of about 10%, in line with computational studies based on the DFT + U method [12, 13].

Growing the mixed metal oxide as a few nanometers thick epitaxial film in a controlled environment would allow a fundamental study of the charge transfer process and may provide further evidence and explanations. In addition, it can offer an alternative prototype material for the reaction because both heat and mass transfer limitations would be largely removed. Many previous works have shown epitaxial films of CeO_2 on metal single crystals such as Ru(0001) [23–25] and Pt(111) [26, 27] surfaces; however, we are not aware of previous attempts related to the epitaxial growth of $Ce_{1-x}U_xO_{2\pm\delta}$ films. Here, we report the *in situ* preparation and characterization of a series of continuous $Ce_{1-x}U_xO_{2\pm\delta}$ (111) thin films of about 6 nm thick

grown on Ru(0001)/Al_2O_3(0001) templates. The reduction of Ce^{4+} cations to Ce^{3+}, as well as U^{4+} oxidation to U^{5+} and U^{6+}, has been quantitatively assessed by their electronic core levels (Ce3d and U4f) through x-ray photoelectron spectroscopy (XPS), while its crystalline quality and stability was studied by low-energy electron diffraction (LEED). A reduction of over 50% of monitored Ce cations by XPS at temperatures as low as 873 K in the absence of a reducing agent (in vacuum) is observed. Similar results were obtained when polycrystalline mixed oxide thin films were grown on nanocrystalline Ru templates deposited on SiO_2/Si wafers. We have also complemented the work with DFT + U calculations of a system in which U substitution of Ce cations was conducted to gauge the extent of reduction of the latter in the mixed oxide. Based on both experimental and computational results, it appears that, in addition to the crucial compositional effect, the distribution of U cations in the CeO_2 matrix (configuration) also affects the extent of reduction.

2. Experimental section

2.1. Epitaxy of $Ce_{1-x}U_xO_2$

Ultrasmooth Ru(0001) thin film templates were grown by magnetron sputtering on sapphire (0001) substrates with a misorientation of less than 0.1° (Crystec), following a similar approach to that reported by several groups [24, 28]. The sputter deposition was performed using a commercial MeiVac MAK magnetron sputtering source with a Ru sputter target (purity 99.99%) installed in a vacuum chamber with a base pressure below 10^{-8} mbar. Before Ru deposition, the sapphire (0001) substrates were cleaned by heating them in vacuum conditions to about 880 K for 20 min. The quality of the Ru(0001) epitaxial thin films, in terms of homogeneity, roughness, and degree of crystallinity, was checked by low-energy electron microscopy using a commercial Elmitec SPELEEM III system with a base pressure better than $\sim 3 \times 10^{-10}$ mbar. Nanocrystalline Ru thin films were grown on SiO_2/Si substrates for comparison.

Epitaxial $Ce_{1-x}U_xO_{2\pm\delta}$(111) thin films were grown and characterized *in situ* at the EU Joint Research Center, laboratory of Properties of Actinide Materials under Extreme Conditions (PAMEC, ActUsLab). The Ru(0001)/Al_2O_3(0001) and Ru/SiO_2 templates were transported under rough vacuum to the JRC and transferred to the PAMEC ultra-high vacuum (UHV) cluster through air. Prior to the deposition of $Ce_{1-x}U_xO_{2\pm\delta}$ films ($x = 0$, 0.05, 0.20, 0.6, and 1), the Ru thin films were cleaned by several cycles of annealing to 873 K in an oxygen background pressure (5×10^{-7} mbar), removing the O_2 during the cooling ramp below 673 K. The surface cleanness and quality were subsequently asserted by LEED and XPS. The $Ce_{1-x}U_xO_{2\pm\delta}$ thin films were prepared *in situ* at a substrate temperature of 673 K by direct current sputtering from metallic cerium and uranium targets in a gas mixture of Ar (6N) and O_2 (6N), with a total pressure of $\sim 6 \times 10^{-3}$ mbar and an O_2 partial pressure limited to 10^{-6} mbar. The growth ratio for each target was initially calibrated under these conditions by growing pure CeO_2 and UO_2 thin films using the same heating power (ca. 1 W), resulting in a similar growth rate of about 0.1 Å s^{-1}, as estimated from XPS measurements. Furthermore, the composition of mixed $Ce_{1-x}U_xO_{2\pm\delta}$ thin films was directly proportional to the relation of heating powers of Ce and U targets, as confirmed by XPS measurements using the corrected atomic sensitivity factors for Ce (Ce 3d), U (U $4f_{7/2}$), and O (O1s) for our XPS analyzer (see below). In all cases, the total power was limited to ca. 1 W to keep the same global growth rate, thus aiming for a total thickness of about 6 nm for depositions of 600 s. As-grown samples were immediately characterized by LEED and XPS. During the present study, thin films were subjected to two thermal treatments. First, samples were subjected to temperature-programmed annealing under UHV conditions (0.5 K s^{-1}, from 190 K to 873 K, i.e. reduction treatment). Secondly, the samples were reoxidized by annealing them at 773 K under an O_2 atmosphere ($\sim 5 \times 10^{-7}$ mbar) for 30 min. After each reduction and reoxidation process, the samples were thoroughly characterized by LEED and XPS.

The whole *in situ* characterization of $Ce_{1-x}U_xO_{2\pm\delta}$ thin films was performed at room temperature in the analysis chamber of the JRC UHV-cluster, which presents a background pressure of 2×10^{-10} mbar. An ErLEED (SPECS) system was used to take LEED patterns at different electron energies varied from 40 to 120 eV. The XPS measurements were performed using a Phoibos 150 hemispherical (SPECS) analyzer equipped with a nine-channeltron detector and Al K_α radiation ($E_{h\nu} = 1486.6$ eV) from a micro-focus source (XRC-1000) operating at 120 W and equipped with a monochromator. The overall energy resolution is about 0.55 eV using a pass energy of 20 eV. The spectrometer was initially calibrated employing the Au $4f_{7/2}$ (83.9 eV binding energy) and Cu $2p_{3/2}$ (932.7 eV binding energy) peaks from clean metallic Au and Cu surfaces, respectively [29]. Sample charging was corrected by employing an electron flood gun (FG 22/35, SPECS) and cross-checking the binding energy scale with internal references (Ru $3d_{5/2}$ at 280 eV [29] and CeO_2 *u*''' peak at 917 eV [30]). After a Shirley background removal, the experimental Ce 3d and U 4f spectra have been fitted by a linear combination of reference Ce 3d and U 4f spectra associated with CeO_2, Ce_2O_3, UO_2, U_2O_5, and UO_3 taken from [30, 31], respectively. The XPS were handled using CasaXPS and XPSpeak 4.2 software. Inelastic peak shape analysis (IPSA) was carried out using the QUASES-Analysis software [32,

33], taking the Ru 3d extended region and a *bulk* Ru(0001)/sapphire(0001) reference sample (>100 nm thick). The electron inelastic mean free path (IMFP) through the $Ce_{1-x}U_xO_{2\pm\delta}$ matrix was calculated using the Tanuma, Powell, and Penn formula IMFP-TPP2M [34].

2.2. Polycrystalline $Ce_{1-x}U_xO_{2\pm\delta}$

A series of polycrystalline mixed oxide $Ce_{1-x}U_xO_{2\pm\delta}$ powders, where $x = 0.05, 0.1, 0.25, 0.5, 0.75$, as well as reference UO_2 and CeO_2, were synthesized by the precipitation method from their precursors: cerium (III) nitrate hexahydrate (Fluka) and uranyl nitrate (BDH Chemicals), at SABIC-KAUST research center. Then, ammonium hydroxide was added until the pH of the solution reached about 9, where cerium and/or uranium hydroxides precipitated. The precipitate was washed with distilled water until neutral pH, dried at 373 K for 12 h, and calcined at 773 K in air for 5 h.

XPS of the polycrystalline samples was conducted using a Thermo Scientific ESCALAB 250 Xi, equipped with a monochromated Al K_α x-ray source, at SABIC-Riyadh Research Center. The base pressure of the chamber was typically in the low 10^{-10} mbar range. Charge neutralization was used for all samples of ~1 eV. Spectra were calibrated to C 1s at 284.7 eV and cross-checked with the CeO_2 component *u*''' at 917 eV [30]. Detailed spectra of regions of interest (U 4f, O 1s, Ce 3d, U 4d, Ce 4d, C 1s, and valence band) were acquired at a pass energy of 20 eV, yielding an analyzer energy resolution of about 0.3 eV. Ar^+ ion bombardment was performed with an EX06 ion gun at 1 kV beam energy and 10 mA emission current with a pressure of ca. 5×10^{-7} mbar; the sample current was typically 0.9–1.0 μA. The sputtered area of 900 × 900 μm^2 was larger than the analyzed area of 600 × 600 μm^2. Self-supported oxide disks of approximately 0.5 cm diameter were loaded into the chamber for analysis. Data acquisition and treatment were performed using the Avantage software.

Transmission electron microscopy (TEM) studies were performed using a Titan ST microscope (FEI company) operated at an accelerating voltage of 300 kV equipped with a field emission electron gun, a 4 k × 4 k CCD camera, a Gatan imaging filter, and a Gatan microscopy suite, at KAUST. The microscope was operated either in high-resolution (HRTEM, phase contrast) or high-angle annular dark field—in scanning TEM (STEM) mode (*Z*-contrast)—with a point-to-point resolution of ca. 0.12 nm. To prepare the TEM sample grid for analysis, a few mg of the oxide were dispersed in ethanol, followed by ultrasonication for 15 min. A drop of supernatant suspension was poured onto a holey carbon-coated Cu grid placed on a filter paper and allowed to dry. Electron energy loss spectroscopy (STEM–EELS) spectra were obtained in the dual-EELS mode, which acquires low-loss (signal from valence electrons) and core-loss (signal from core–shell electrons). Images of the elemental maps in the Supporting Information are generated using STEM-EDS techniques and energy-filtered TEM (EFTEM). The EFTEM-based method for map generation is called the 'jump-ratio method', in which the post-edge image is divided by the pre-edge image to generate the elemental map of Ce, U, and O atoms.

Thermal water splitting reactions were conducted in a quartz reactor connected through an injection valve to a GC equipped with a thermal conductivity detector for hydrogen detection. A Porapack packed column 2 m long, 0.317 cm outer diameter was used at 320 K in isotherm mode and with N_2 flow (20 ml min^{-1}) as the carrier gas for the analysis. Water (steam), placed in a saturator (at room temperature, 23 Torr or about 3% at 1 atm.) before the reactor, was introduced using N_2 flow of 120 ml min^{-1}. The mixed oxide weight was typically 250 mg. The mixed oxide was reduced under an H_2 flow at one atmosphere at 973 K for several hours, then purged with N_2 at the same temperature for about 30 min before starting the reaction. The reaction typically lasted 30 min, and the total amount of hydrogen produced was integrated for each mixed oxide.

2.3. Computation

Periodic density functional theory (DFT) calculations were performed using the Vienna Ab initio Simulation Package [35, 36]. The Perdew–Burke–Ernzerhof functional [37], based on the generalized gradient approximation (GGA), was employed to describe the exchange–correlation energy. The interactions between the valence electrons and the ionic cores were treated using the projector augmented wave method [38]. In particular, to account for the strong on-site Coulomb repulsion of the localized Ce 4f and U 5f, we applied the GGA + U approach formulated by Dudarev and co-workers [39]. Similar to the previous work simulating the ceria–urania solid solution [12], $U_{eff} = 5.0$ and 4.0 eV for Ce and U were used. We first optimized the cubic fluorite structure of CeO_2 and UO_2 to model the bulk structures. For the pure UO_2 model, we applied antiferromagnetism to align with previous results [40] and accurately describe the electronic structures. All calculations were conducted with a kinetic energy cut-off of 415 eV for a plane wave basis set after ensuring sufficient convergence. The Brillouin zone was sampled using Monkhorst–Pack meshes [41] with a (3 × 3 × 3) *k*-point grid for bulk calculations. Solid solutions with 3.1% and 6.2% uranium were modeled by substituting uranium atoms into the ceria (2 × 2 × 2) bulk structure,

corresponding to 1/32 and 2/32 substitutions, respectively. Similar to previous studies [42], one oxygen vacancy (V_O) was created from the perfect ceria structure containing 96 atoms (32 Ce and 64 O), positioned adjacent to the dopant U atom (see figure S1 in the supporting information). The oxygen-vacancy formation energy (E_{VO}) is calculated by the following equation:

$$E_{V_O} = E_{Ce_{31}UO_{63}} + \frac{1}{2}E_{[\text{triplet } O_2]} - E_{Ce_{31}UO_{64}}. \quad (4)$$

To systematically investigate the effects of uranium ion positions and the charge transfer mechanism, a ($4 \times 2 \times 1$) model was applied. In addition, high U concentrations (25%, 50%, and 75%) with a ($1 \times 1 \times 1$) model were analyzed to align with experimental observations. The defect structures were fully optimized after optimizing the bulk structures for pure CeO_2, UO_2, and their solid solutions.

3. Results and discussion

3.1. Polycrystalline $Ce_{1-x}U_xO_2$

A series of polycrystalline $Ce_{1-x}U_xO_{2\pm\delta}$ was previously synthesized and studied for their TCWS to hydrogen [21]. Briefly, x-ray diffraction (XRD) measurements have shown that as-prepared mixed oxides present a fluorite structure, in line with numerous other studies in which Ce and U cations have high miscibility [43–45]. This miscibility, however, may break down with temperature. For example, in the case of $Ce_{0.5}U_{0.5}O_2$, heating to 750 K or above in the XRD cell resulted in the formation of small amounts of uranium oxide in a different phase; weak diffraction patterns attributed to either U_2O_5 (U^{5+}) or U_3O_8 (U^{5+} and U^{6+}) were observed. Here, we present HRTEM/EELS as an example of one of the studied fresh mixed oxides ($Ce_{0.75}U_{0.25}O_2$). Figure 1(A) (HRTEM) shows the particles to be of a crystalline nature with a crystallite size of about 10 nm. Extensive TEM, STEM, EDX, and EELS have been conducted for two samples ($Ce_{0.75}U_{0.25}O_2$ and $Ce_{0.95}U_{0.05}O_2$; see supporting information Figures S2–S5 for $Ce_{0.95}U_{0.05}O_2$). All data point to the high miscibility of U cations in CeO_2. For example, while figure 1(B) (STEM) shows no distinction between the atoms, the EELS spectrum of the same area, displayed in figure 1(C), shows the presence of both U and Ce, as evidenced by the Ce 3d ➔ 4f and U 4d ➔ 5f transitions. Also, the lattice fringes obtained from the diffraction pattern (figure 1(d)) related to figure 1(B) are nearly identical to those of CeO_2.

The TCWS to hydrogen at 973 K for the series $Ce_{1-x}U_xO_{2\pm\delta}$ (where $0.05 \leqslant x \leqslant 0.75$, including pure CeO_2 and UO_2) was further studied to unravel the effect of substituting Ce^{4+} by U^{4+} cations on the reaction. The runs were conducted until the reaction was completed, which took about 30 min. For example, figure 2(A) presents a plot of the hydrogen production from water (vapor pressure 23 torr) as a function of time over prior reduced $Ce_{0.95}U_{0.05}O_2$. Besides, the calculated total hydrogen production per weight at 973 K over these oxides is presented in figure 2(B). The pure oxides present a small activity at both ends of the plot. The presence of U in small amounts resulted in considerable enhancement of hydrogen production (about 30 times compared to CeO_2). Increasing the amounts of U, while still showing enhancement compared to CeO_2, was detrimental, as seen in figure 2(B). In addition, the figure presents the percentage of Ce^{3+} states (as obtained from XPS Ce 3d lines [21]) that were produced upon Ar-ions sputtering of the same polycrystalline mixed oxide series. The trend is similar to hydrogen production: substituting Ce by U cations increased the reduction of Ce^{3+} considerably. Figure 2(C) presents some of the data of the hydrogen production shown in figure 2(B) as a function of bulk oxygen vacancy formation energy that was previously computed using DFT + U (U_{eff} = 4 eV for U and 5 eV for Ce) on a CeO_2 cell (that contained 4 Ce cations) in which one, two, or three U cations substituted for Ce cations to give 0.25, 0.5 and 0.75 U composition, in addition to CeO_2 and UO_2 [13]. The introduction of U considerably decreased the energy needed to remove bulk oxygen atoms. The effect is, however, offset by increasing U content, presumably because it is harder to reduce U^{4+} cations.

To summarize this section, the above results indicate that the presence of U cations in small amounts enhances the reduction of Ce^{3+} (XPS) (i) by decreasing the energy needed to remove lattice oxygen (DFT + U) (ii), thus increasing the TCWS of the mixed oxide (test reactions) (iii).

3.2. Epitaxy $Ce_{1-x}U_xO_2$

The growth of (111)-oriented CeO_2 on Ru(0001) by molecular beam epitaxy has been extensively studied, determining a relationship between substrate temperature and ceria morphology [25]. Limiting the growth temperature to 673 K results in a continuous epitaxial (111) thin film, thus minimizing the influence of the CeO_2 islands morphology on the Ce^{3+}/Ce^{4+} ratio (i.e. potential higher reduction at the nanoisland borders). Figure 3 shows the characteristic LEED pattern of (111)-oriented epitaxial thin films for all $Ce_{1-x}U_xO_{2\pm\delta}$ stoichiometries. Samples with low U content present a faint ring associated with a small fraction of randomly

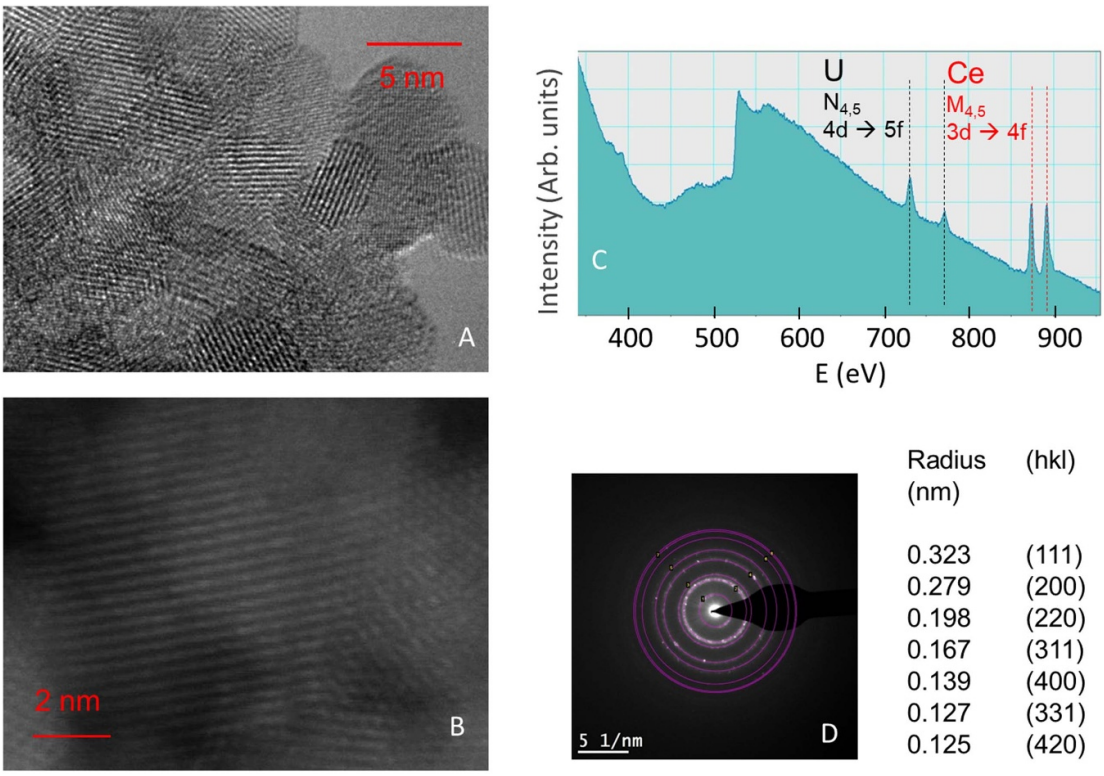

Figure 1. (A). High-resolution transmission electron microscopy (HRTEM) of $Ce_{0.75}U_{0.25}O_2$ polycrystalline mixed oxide. (B). Scanning transmission electron microscopy (STEM) of a selected area from (A). (C). Electron energy loss spectroscopy (EELS) spectrum of the area shown in (B). (D). Selected area electron diffraction (SAED) of (B).

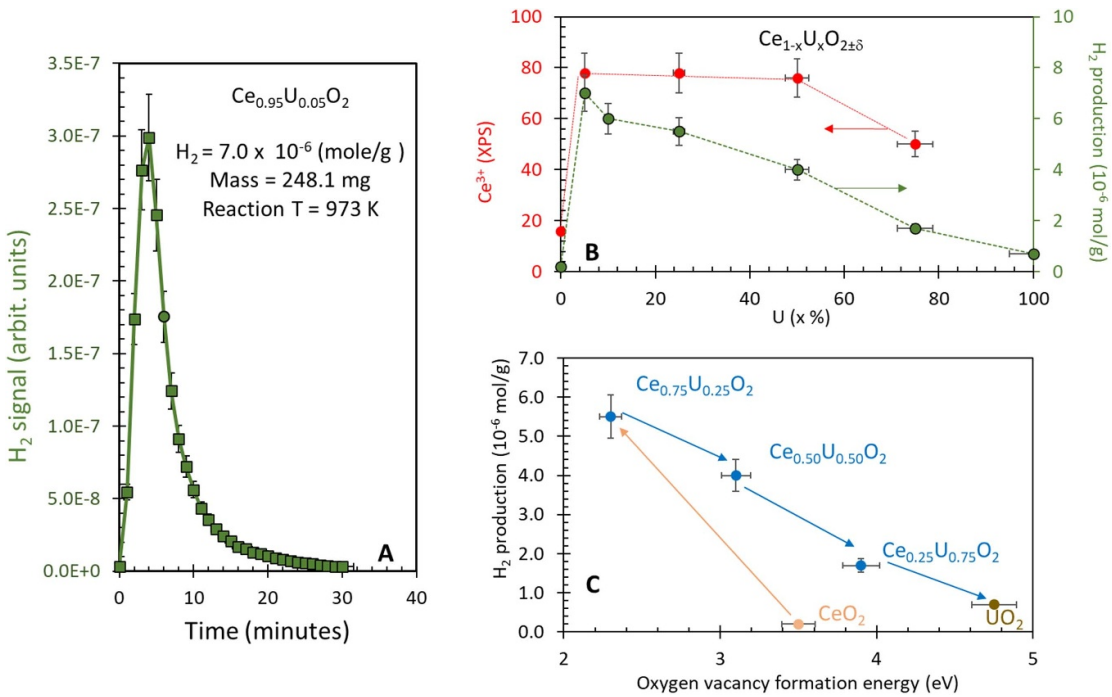

Figure 2. (A). Thermochemical water splitting (TCWS) at 973 K on pre-reduced (H_2, 973 K) $Ce_{0.95}U_{0.05}O_2$; water vapor = 23 torr in N_2 with a flow rate = 120 ml min^{-1} at one atm. (B). Hydrogen production during TCWS on a series of $Ce_{1-x}U_xO_{2\pm\delta}$ mixed oxide as a function of U content (right *y*-axis). The percentage of Ce^{3+} (XPS Ce3d lines from [21]) cations obtained upon reduction with Ar-ions prior to XPS collection at room temperature is shown in the left *y*-axis. (C). Hydrogen production on a selected number from the series presented in B as a function of oxygen vacancy formation computed using DFT + U (5 eV)[13].

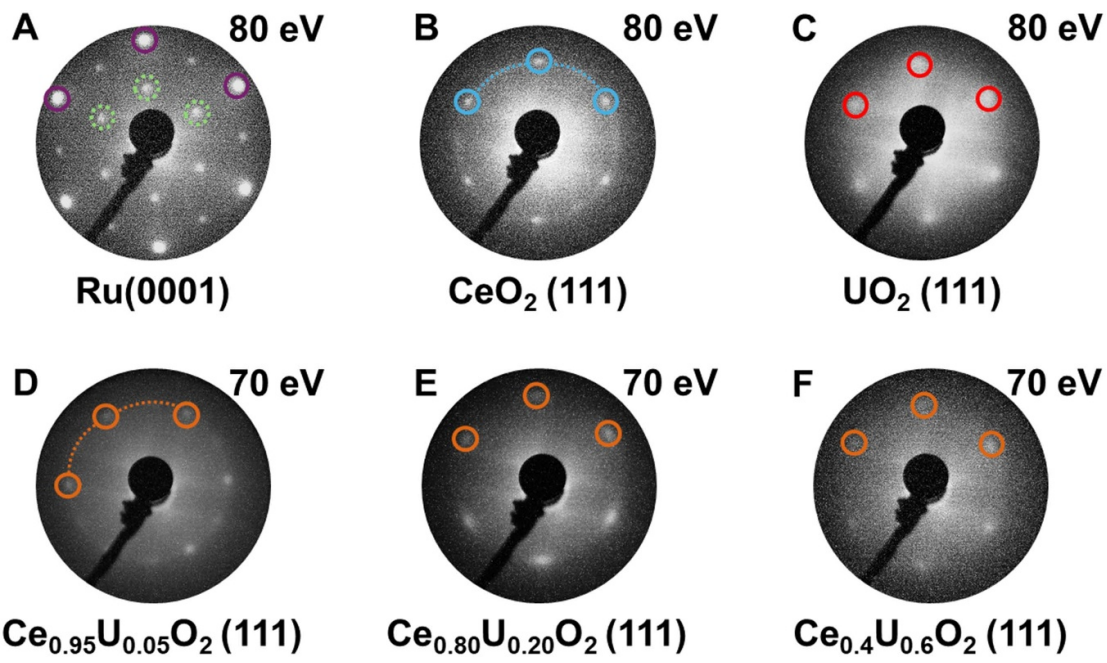

Figure 3. LEED patterns taken at room temperature. (A). Clean Ru(0001)/Al_2O_3(0001) substrate. The hexagonal pattern indicated by solid violet circles corresponds to the Ru spots, while the dashed green circles indicate the (2 × 1) reconstruction of adsorbed oxygen. (B). and (C)., CeO_2 and UO_2 (111) reference thin films, where solid circles (blue and red, respectively) indicate their spots in azimuthal registry with the Ru(0001). For the CeO_2 pattern, the dashed blue arc indicates the faint ring associated with a small fraction of randomly oriented islands. (D)–(F). LEED patterns of $Ce_xU_{1-x}O_{2\pm\delta}$ thin films with $x = 0.05$, 0.2, and 0.6, respectively. Solid orange circles indicate their spots in azimuthal registry with the Ru(0001).

oriented islands, while the increase of U translates into a blurring of the spots and an increase in the background, which indicates a higher disorder and density of structural defects. The absence of Ru(0001) spots indicates a complete coverage of the whole substrate, as confirmed by the XPS IPSA (see figure S6).

In situ XPS measurements of Ce 3d and U 4f regions allow monitoring the Ce and U cations degree of oxidation on the epitaxial $Ce_{1-x}U_xO_{2\pm\delta}$ thin films. Figures 4(A) and (B) presents the XPS Ce 3d and U 4f lines for CeO_2 and UO_2 reference thin films, respectively. There is a marginal difference in the XPS Ce 3d (U 4f) lines for the as-prepared film and the one annealed to 873 K; therefore, the signal from the as-prepared films is omitted for simplicity. As can be seen for the $CeO_{2-\delta}$ film, the Ce 3d lines are qualitatively dominated by the Ce^{4+} cations ($v = 882.6$ eV, $v'' = 898.7$ eV, and $u'' = 916.9$ eV) for the UHV annealed film. The small contribution from Ce^{3+} cations (v' ca. 886 eV) vanishes upon heating in O_2 (5×10^{-7} mbar). For the UHV annealed UO_2 film, the XPS U 4f spectra indicate the presence of mostly U^{4+} cations (U $4f_{7/2} = 380.2$ eV and its satellite at 6.9 eV above). Heating it in the presence of O_2 resulted in the oxidation of a nonnegligible fraction of U^{4+} cations to U^{5+} cations ($U4f_{7/2} = 381.1$, $U4f_{5/2} = 391.8$ and its satellite at ca. 8 eV above; note that the U $4f_{5/2}$ component of the U^{4+} cations obscures the $U4f_{7/2}$ satellite of the U^{5+} cations) [46]. Therefore, it is clear that the UHV annealed films are mostly composed of Ce^{4+} (for CeO_2) and exclusively composed of U^{4+} (for UO_2). Annealing in O_2 resulted in the oxidation of a small fraction of Ce^{3+} in CeO_2 but in a considerable conversion of U^{4+} to U^{5+} in 'formerly' UO_2. A detailed description of XPS fitting results, performed by a linear combination of reference spectra and corresponding estimated Ce^{4+}/Ce^{3+} and $U^{4+}/U^{5+}/U^{6+}$ relative percentages, as well as Ce, U, and O atomic concentrations, can be found in the Supporting information, figures S7 and S8 and table S1.

3.2.1. Evidence of charge transfer

A noticeable difference is seen for the mixed oxide thin film samples. Figures 5(A) and (B) presents the same XPS regions as those shown in figure 4 for the $Ce_{0.8}U_{0.2}O_{2\pm\delta}$; the $Ce_{0.95}U_{0.05}O_{2\pm\delta}$ is presented in figure S9. XPS Ce 3d indicates (figure 5(A)) that the UHV annealed film now comprises a significant fraction of Ce^{3+} (which was not observed for $CeO_{2\pm\delta}$); the estimated ratio Ce^{3+}/Ce^{4+} is equal to 2.7 (table S1). Besides, the XPS U 4f lines of the same film contain a large fraction of U^{5+} (UHV annealed of UO_2 alone did not contain U^{5+}), where the U^{5+}/U^{4+} was found equal to 1.5. Similar trends were obtained for other investigated mixed oxides, yet quantitative differences were observed. Before addressing these and their importance within the context of the TCWS, it is worth indicating the following: the charge transfer occurs during the annealing process (as indicated by equation (3)). Equally important, heating in O_2 resulted in preferential oxidation

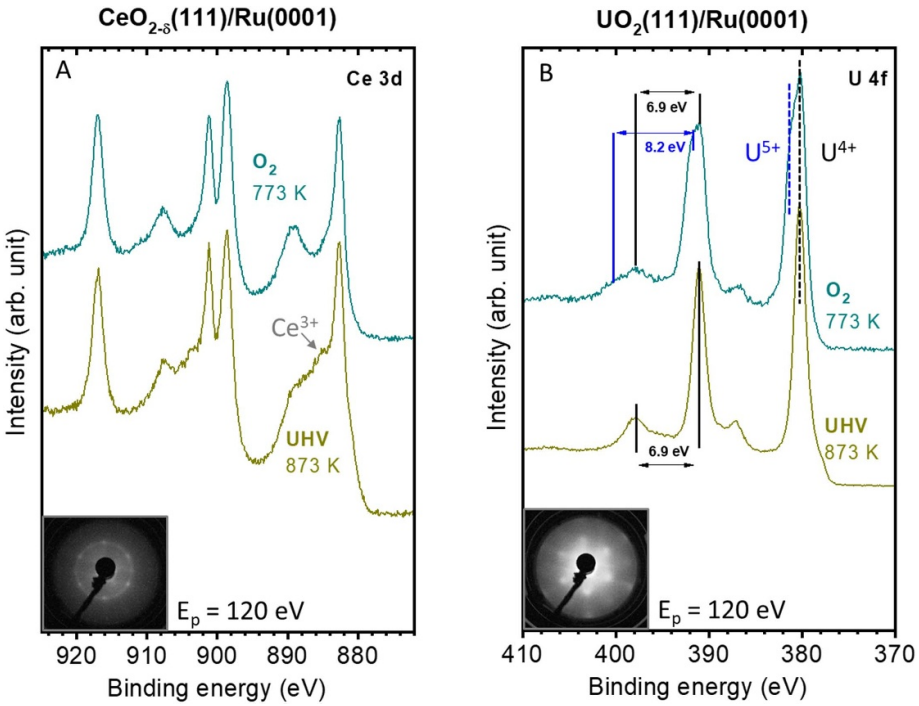

Figure 4. (A). XPS Ce 3d of CeO_2 thin film after annealing in vacuum (bottom) and heating in 5×10^{-7} mbar O_2 for 30 min (top). (B). XPS U 4f of UO_2 thin film after annealing in vacuum (bottom) and heating in 5×10^{-7} mbar O_2 for 30 min (top). The insets show the LEED image of the UHV annealed films.

back to Ce^{4+}, yet it seems that under these conditions, part of the oxygen consumed for the oxidation was transferred from U^{5+} because the oxidation trend has reversed (as seen in figure 5(B)). Therefore, the dynamic of the electron transfer between both metal cations is sensitive to the partial pressure of O_2 in addition to the Ce to U ratio and possibly relative positions in the lattice. In this study, the O_2 pressure was kept constant during the reoxidation step for all samples (5×10^{-7} mbar).

3.2.2. Possible structural effect

Focusing on the U cations, at low atomic percentage (figure S9 for the 5%; $Ce_{0.95}U_{0.05}O_2$), most are in a +5 oxidation state upon reduction (UHV annealed). Increasing the percentage of U to about 20% decreased the fraction of oxidized U cations (figure 5). Further increasing the U content resulted in only negligible oxidation to +5. This result is presented in figures 6(A) and (B), in which the number of U cations was close to that of Ce cations ($Ce_{0.4}U_{0.6}O_2$). While the ratio Ce^{3+}/Ce^{4+} decreased compared to that of the lower U content, it was still high. This trend indicates that the reduction of Ce^{4+} when U cations content is significant is not solely explained by the charge transfer described in equation (3). It is also unrelated to the size effect, as in the case of Zr^{4+} cations (compensation for lattice expansion) [47]; Ce^{4+} and U^{4+} cations have a similar size (ca. 1 Å). Inspection of the same sample (figure 6(A)) indicates that Ce^{3+} cations were still present even when heated in O_2, while U cations were oxidized to U^{5+} and a small fraction to U^{6+} (figure 6(B)). As mentioned above, previous works on polycrystalline $Ce_{0.5}U_{0.5}O_2$ showed segregation of the uranium oxide [21] with heating, moving away from the fluorite structure with diffraction lines that are attributed to either/or U_2O_5 and U_3O_8. Taking these observations together and the fact that UO_2 tends to become UO_{2+x}, one may conclude that it may segregate to the top of the thin film, shielding CeO_2 from being oxidized, and that is why Ce^{3+} cations are still present even when the film was annealed in the presence of O_2. This will have a detrimental effect on the activity of the TCWS. While Ce^{3+} cations are formed, when the percentage of U cations is high, although proportionally less than the other films, they will not be as active because they are in deeper layers, thus explaining the decrease of the activity with increasing U content after the optimal concentration, as seen in figure 2(B). Therefore, there is no incentive to make a mixed oxide with a large fraction of U cations because phase segregation may occur in addition to the dilution effect.

To check for the redox cycle, an oxidized $Ce_{0.8}U_{0.2}O_{2\pm\delta}$ film, which was stored in UHV after the previous thermal treatments, was analyzed again and subsequently heated in UHV (4×10^{-10} mbar) to 873 K. Figure S10 shows that Ce^{4+} reduction to Ce^{3+} and U^{4+} oxidation to U^{5+} occurred again, as expected. Therefore, at least when the U content is low, the thin film showed a repeating cycle behavior, which is needed for the TCWS reaction to occur.

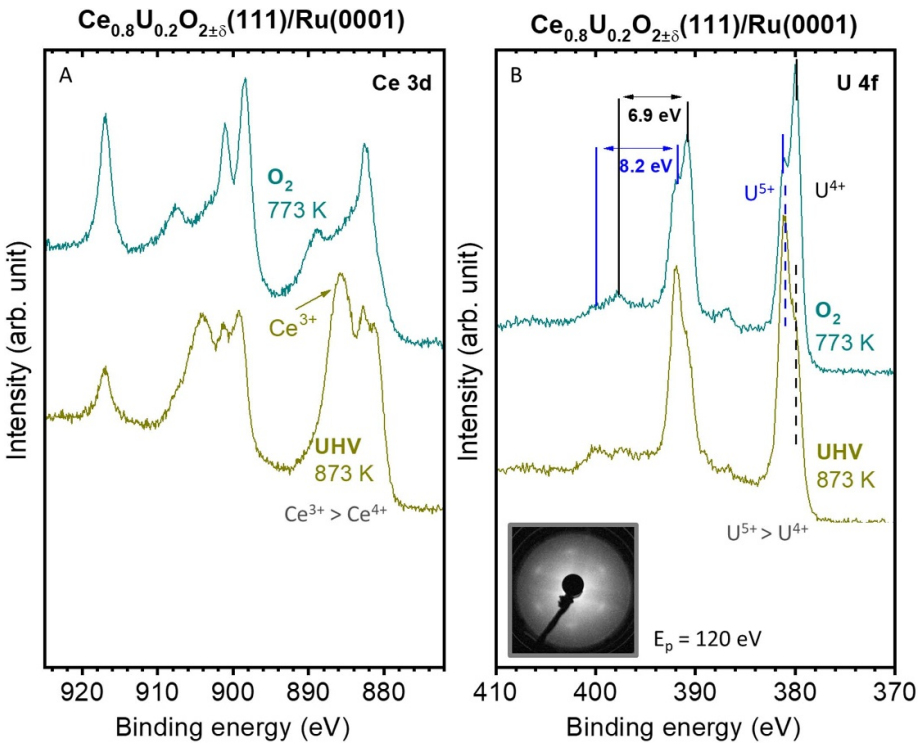

Figure 5. (A). XPS Ce 3d of $Ce_{0.8}U_{0.2}O_{2\pm\delta}$ thin film after annealing in vacuum (bottom) and heating in 5×10^{-7} mbar O_2 for 30 min (top). (B). XPS U 4f of $Ce_{0.8}U_{0.2}O_{2\pm\delta}$ thin film after annealing in vacuum (bottom) and heating in 5×10^{-7} mbar O_2 for 30 min (top). The inset shows the LEED image of the UHV annealed film.

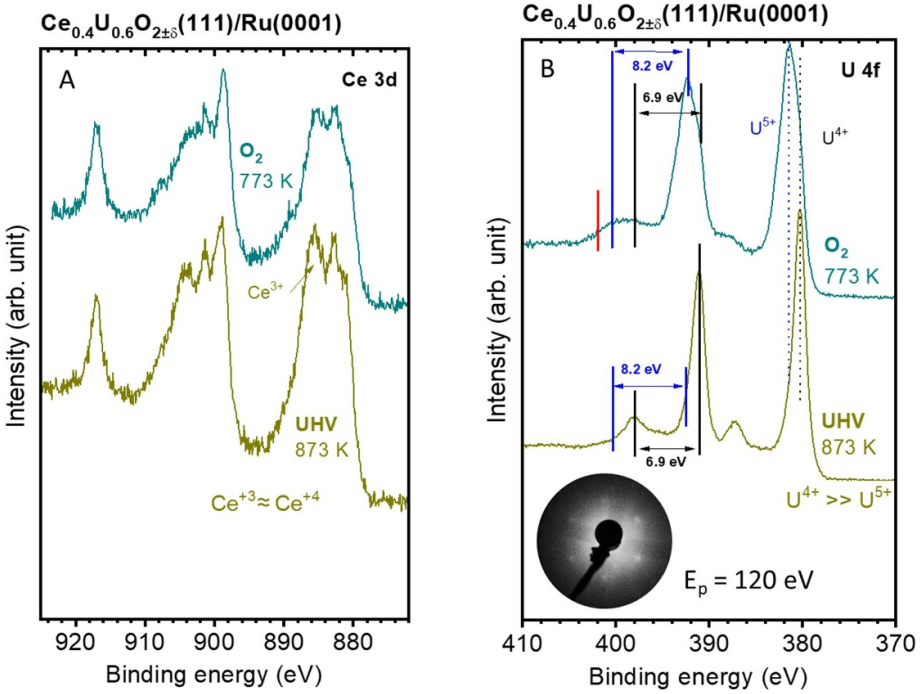

Figure 6. (A). XPS Ce 3d of $Ce_{0.4}U_{0.6}O_{2\pm\delta}$ thin film after annealing in vacuum (bottom) and heating in 5×10^{-7} mbar O_2 for 30 min (top). (B). XPS U 4f of $Ce_{0.4}U_{0.6}O_{2\pm\delta}$ thin film after annealing in vacuum (bottom) and heating in 5×10^{-7} mbar O_2 for 30 min (top). The inset shows the LEED image of the UHV annealed film. The red line is at the position of a U^{6+} satellite; this, together with the large FWHM of the main lines ($U4f_{7/2,5/2}$), indicates that U cations have a wide range of oxidation states from +4 to +6.

Furthermore, a thin film of the mixed oxide ($Ce_{0.8}U_{0.2}O_{2\pm\delta}$) was prepared on an amorphous Ru substrate to test for differences to the epitaxially grown film, as it represents a structural intermediate between the single crystalline-like structure and the polycrystalline one (figure S11). The film on the

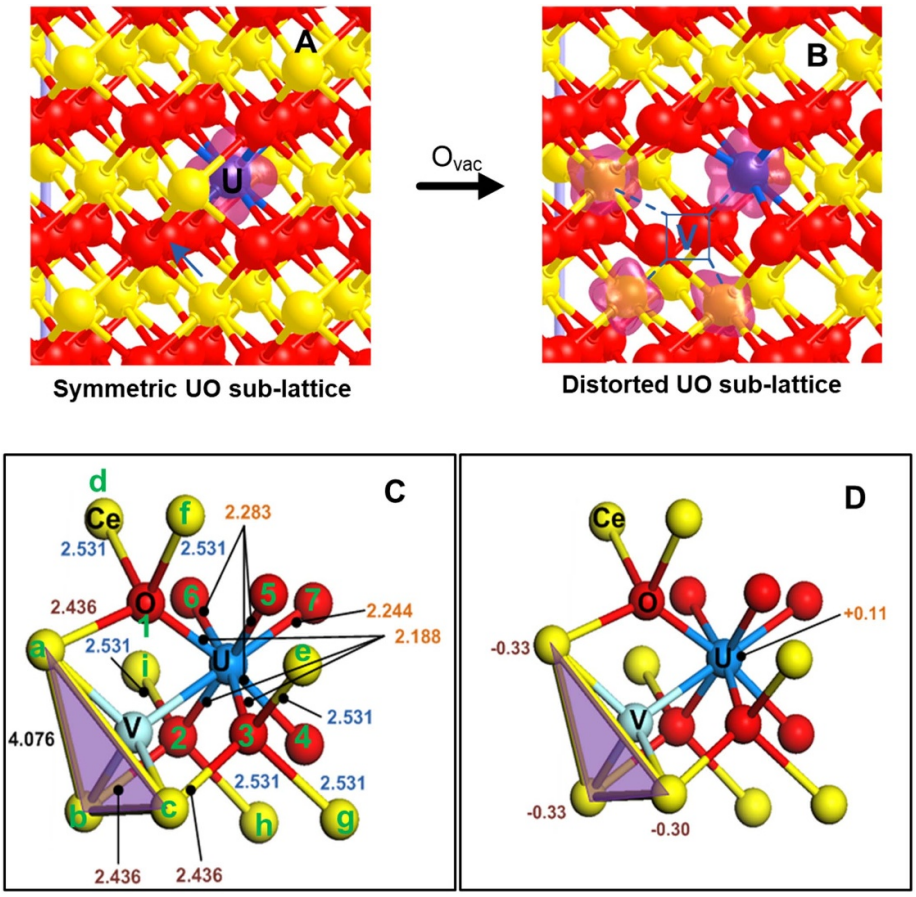

Figure 7. (A). A section of the super cell ($Ce_{1-x}U_xO_2$: (2 × 2 × 2) model (31 Ce, 1 U, and 64 O atoms); U % = 3.1%) showing the U cation (purple), Ce cations (yellow) and oxygen anions (red). The arrow points to the oxygen ion to be removed. Note the 5f orbitals of the U^{4+} cation that contain two electrons and the absence of 4f electrons on the Ce^{4+} cations. (B). The same section as in A after removing the oxygen anion. Three Ce cations have accommodated one electron each in their 4f states, while the U cation has lost one electron. (C). Bond distances of the Ce and U cations adjacent to the oxygen vacancy (note that Ce–O and U–O distances of the stoichiometric cells are Ce–O = 2.372 Å and U–O = 2.342 Å). (D). Bader charges on the three Ce cations and U cation in the presence of the oxygen vacancy. See table S2 for further analysis of C.

amorphous Ru substrate responded similarly to the single crystalline ones. Upon annealing in UHV, the reduction of Ce^{4+} to Ce^{3+} and the oxidation of U^{4+} to U^{5+} was clear. Also, as for the other films, heating in O_2 reversed the process.

3.2.3. Computation: charge transfer and effect of U cations locations

Figure 7 (A) and (B) presents the results of the DFT + U computation of $Ce_{31}UO_{64}$ before and after creating an oxygen vacancy to make a $Ce_{31}UO_{63}$ super-cell. There are no Ce 4f electrons before the removal of the oxygen ion, while three electrons on three Ce cations (Ce4f orbitals) are seen after the creation of the oxygen vacancy. Therefore, removing an oxygen ion from the lattice resulted in the expected transfer of two electrons towards two Ce^{4+} cations (undoped ceria case), plus the additional reduction of a third Ce^{4+} cation to Ce^{3+} due to the charge transfer from U^{4+} to become U^{5+}. Figures 7 (C) and (D) presents the bond distances between Ce (U) and oxygen ions and the Bader charge analysis in the presence of an oxygen vacancy. Contraction in the U–O bonds and expansions in the Ce–O bonds are noticed. A detailed description is presented in table S2, where the focus is made on the bonds of seven oxygen ions with Ce and U cations (the oxygen atoms are labeled 1–7). Ce^{3+} cations directly adjacent to the vacancy experience an expansion in their bond distance to the nearest oxygen by 2.7%. Yet, Ce^{4+} cations adjacent to the nearest oxygen atoms, labeled $Ce_{d\text{-}i}$, experience an even larger bond distance expansion of 6.7%. The U^{5+} cation shows a contraction of its bond distances to the seven oxygen ions. The contraction is, however, non-symmetric and spans from 2.5 to 6.6%, as seen in table S2.

To test the configurational effect of U cations on the reduction of Ce^{4+} cations, we performed runs in which U cations with the same concentration had two different initial positions. It is being taken in mind that both the thin film and polycrystalline oxides have shown that there is no incentive to increase the concentration of U beyond a certain limit as the system becomes dominated by the uranium oxide and is,

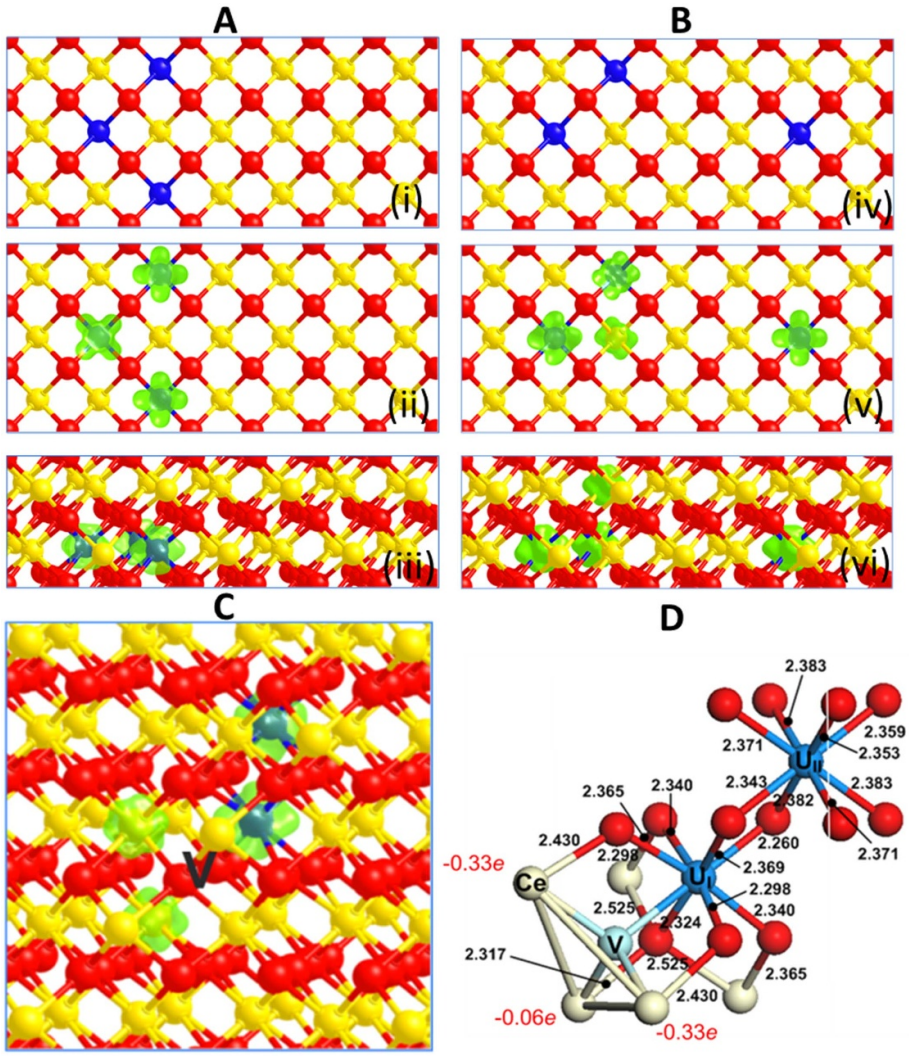

Figure 8. (A). and (B). Effect of U arrangement around Ce ions on electron transfer. U concentration is 9.3% doping of the (4 × 2 × 1) bulk model ($Ce_{29}U_3O_{64}$ ($Ce_{0.907}U_{0.093}O_2$)). (i) and (iv) U, Ce, and O are in blue, yellow, and red; top view. (ii) and (v) Projected orbitals on U and Ce ions; top view. (iii) and (vi) Projected orbitals on U and Ce ions; side view. (C). Effect of U arrangement around to Ce ions on electron transfer. U concentration is 6.2% doping of the (2 × 2 × 2) bulk model ($Ce_{30}U_2O_{63}$ ($Ce_{0.937}U_{0.063}O_{1.969}$)) in the presence of an oxygen vacancy. (D). Bond distances and Bader charge on Ce in the presence of an oxygen vacancy (from C).

therefore, largely non-reducible. Figures 8(A) and (B) presents results from a super cell (4 × 2 × 1) containing 3 U cations of a $Ce_{29}U_3O_{64}$ ($Ce_{0.907}U_{0.093}O_2$). The three U-cations were configured differently. In one case (8 A) they are surrounding a Ce^{4+} cation, thus representing a high local concentration (the shaded rectangle in the figure corresponds to U cations = 3/5 in 2D or 3/16 in 3D), while in the second case one (8 B) of the three cations is moved three units to the left on the *x*-axis and one unit up on the *y*-axis (a unit is defined as the Ce^{+4} to Ce^{+4} distance, which is equal to 3.86 Å). No electron transfer occurred in the first configuration, while in the second, in which only two U cations were adjacent to Ce^{4+}, transfer did occur to the Ce cation at equidistance from the two U cations. Figures 8(C) and (D) presents a specific case of figure 8(B), in which the slab contains the two U cations adjacent to one Ce^{4+} cation and where electron transfer did occur. The removal of an oxygen ion in this case did not result in the formation of three Ce^{4+} but in two, as if the U cations were absent. In this case, the presence of the two U cations adjacent to each other prevented the charge transfer upon the removal of an oxygen ion, as evidenced by the much less bond contraction of U_I (when compared to those presented in figure 7) and U_{II} (the one furthest away from the vacancy had a negligible change in bond distances). Investigating a model system with atomic resolution would be needed to support the computational results further; however, the weak electrical conductivity of both oxides represents a considerable challenge for performing scanning tunneling spectroscopy (STM) of single crystals. Nevertheless, the epitaxial thin oxides of this work may have the electrical conductivity needed for future STM studies.

Based on the above results on polycrystalline and epitaxial $Ce_{1-x}U_xO_2$ samples, charge transfer from U to Ce cations occurs. Its extent, however, has a considerable entropical factor. Low concentrations of U cations are needed, and this is not solely related to a dilution effect. Moreover, the analysis of model $Ce_{1-x}U_xO_2(111)$ thin films indicates that the fraction of Ce^{4+} reduction to Ce^{3+} is larger than that of U^{4+} oxidation to U^{5+} (or U^{6+}) by a factor far exceeding experimental uncertainties. This is rationalized by the possibility that, at high U concentrations, the U cations migrate to the shell of the crystallites. Besides the fact that UO_2 is easily oxidized to higher oxidation states, O_2 adsorption on $UO_2(111)$ is possible (with a computed adsorption energy of −0.24 eV) [48], whereas there are no known experimental reports of irreversible O_2 adsorption on $CeO_2(111)$. Together, these facts would result in a core–shell structure ($UO_y/Ce_{1-z}U_zO_2$), preventing Ce^{3+} cations from being oxidized in the core of the crystallite. Such element migration and phase separation are not uncommon in metallic nanoparticles; for example, an alloy of RhPd or RhPt particles sees surface segregation of Rh to the surface in an oxidized environment [49] because it is easier to oxidize Rh when compared to Pt or Pd. The reduction of Ce cation in the presence of U cations, while it seems to occur via charge transfer, is therefore very sensitive to the configuration of the metal cations, and, as pointed out computationally before [12], its energy is sensitive to statistical entropy contribution.

4. Conclusions

TCWS to hydrogen over polycrystalline and single crystalline $Ce_{1-x}U_xO_2$ is sensitive to the content of U. The polycrystalline mixed oxide was found to be homogeneous as investigated by HRTEM, EELS, and SAED, while the single crystalline (made by epitaxial growth over Ru(0001)) was predominantly (111) terminated. Low percentages of U cation considerably enhanced hydrogen production from water. This enhancement is tracked down to the increase in Ce^{4+} cations reduction to Ce^{3+} cations. The trend of this Ce^{4+}/Ce^{3+} conversion studied by *in situ* XPS showed evidence of charge transfer ($Ce^{4+} + U^{4+} \rightarrow Ce^{3+} + U^{5+}$) at low U content. However, while high atomic percentages of U (20%–60%) decreased the charge transfer efficiency, they protected reduced Ce^{3+} from being oxidized by U diffusion to the outer layers, thus forming oxidized UO_x phases. Evidence of charge transfer was further obtained computationally using the DFT + U method, which occurred at 3.5 and 6.2 at.% of U, explaining the experimental Ce^{4+}/Ce^{3+} and $U^{4+}/U^{5+}/U^{6+}$ results as a function of U content and applied thermal treatment. This charge-transfer effect is, however, sensitive to the distribution of U^{4+} cations around Ce^{4+}. For example, no charge transfer occurred when three U^{4+} cations surrounded one Ce^{4+} atom, while decreasing the number to two showed evidence of charge transfer in the absence of an oxygen vacancy. Besides, in the latter scenario, no further Ce^{4+}/Ce^{3+} conversion occurs after the formation of one oxygen vacancy, as expected for pure CeO_2. Furthermore, when only one Ce^{4+} atom is substituted by U^{4+}, the charge transfer is only manifested when an oxygen vacancy is formed; thus, three Ce^{3+} cations appear instead of the expected two of a CeO_2 matrix. Therefore, the results of this work are best explained by the entropical effect. In a mixed metal oxide, cations distribution matters in addition to their relative fraction. The results of this work are poised to help design more efficient reducible materials where the presence of oxygen vacancies is important, as is the case for the thermal hydrogen production from water.

Data availability statement

All data that support the findings of this study are included within the article (and any supplementary files).

Acknowledgments

The experimental data used in this research were generated through access to the ActUsLab/PAMEC under the Framework of access to the Joint Research Centre Physical Research Infrastructures of the European Commission ($Ce_{1-x}U_xO_2$_Cat_CO2, Research Infrastructure Access Agreement N°36619/08). Part of this work has been supported by the Federal Ministry of Education and Research of Germany (BMBF) within the iCampus2 project, Grant Number 16ME0420K. One of the authors (C Morales) thanks the Postdoc Network Brandenburg for a PNB individual grant. One of the authors (R Tschammer) acknowledges the funding by BTU in the framework of the BTU-BAM Graduate School 'Trustworthy Hydrogen'. The authors thank Y Alsalik (SABIC R&D) for preparing the polycrystalline material and for conducting part of the XPS data acquisition and analysis.

Conflict of interest

The authors declare no conflict of interest.

ORCID iDs

Carlos Morales https://orcid.org/0000-0001-5890-1950
Rudi Tschammer https://orcid.org/0009-0004-6036-1331
Dalaver Anjum https://orcid.org/0000-0003-2336-2859
Aman Baunthiyal https://orcid.org/0009-0001-0312-5082
Jan Ingo Flege https://orcid.org/0000-0002-8346-6863
Hicham Idriss https://orcid.org/0000-0001-8614-7019

References

[1] Pinto F M, Suzuki V Y, Silva R C and La Porta F A 2019 Oxygen defects and surface chemistry of reducible oxides *Front. Mater.* **6** 260
[2] Lin T, Lv X, Hu Z, Xu A and Feng C 2019 Semiconductor metal oxides as chemoresistive sensors for detecting volatile organic compounds *Sensors* **19** 233
[3] Chueh W C, Falter C, Abbott M, Scipio D, Furler P, Haile S M and Steinfeld A 2010 High-flux solar-driven thermochemical dissociation of CO_2 and H_2O using nonstoichiometric ceria *Science* **330** 1797–801
[4] Millican S L, Androshchuk I, Tran J T, Trottier R M, Bayon A, Al Salik Y, Idriss H, Musgrave C B and Weimer A W 2020 Oxidation kinetics of hercynite spinels for solar thermochemical fuel production *Chem. Eng. J.* **401** 126015
[5] Idriss H 2022 Oxygen vacancies role in thermally driven and photon driven catalytic reactions *Chem. Catal.* **2** 1549–60
[6] Montini T, Melchionna M, Monai M and Fornasiero P 2016 Fundamentals and catalytic applications of CeO_2-based materials *Chem. Rev.* **116** 5987–6041
[7] Etim U J, Song Y and Zhong Z 2020 Improving the Cu/ZnO-based catalysts for carbon dioxide hydrogenation to methanol, and the use of methanol as a renewable energy storage media *Front. Energy Res.* **8** 545431
[8] Taniya K, Horie Y, Fujita R, Ichihashi Y and Nishiyama S 2023 Mechanistic study of water–gas shift reaction over copper/zinc-oxide/alumina catalyst in a reformed gas atmosphere: influence of hydrogen on reaction rate *Appl. Catal.* B **330** 122568
[9] Gálvez M E, Jacot R, Scheffe J, Cooper T, Patzke G and Steinfeld A 2015 Physico-chemical changes in Ca, Sr and Al-doped La–Mn–O perovskites upon thermochemical splitting of CO_2 via redox cycling *Phys. Chem. Chem. Phys.* **17** 6629–34
[10] Bulfin B, Lowe A J, Keogh K A, Murphy B E, Lübben O, Krasnikov S A and Shvets I V 2013 Analytical model of CeO_2 oxidation and reduction *J. Phys. Chem.* C **117** 24129–37
[11] Andersson D A, Simak S I, Skorodumova N V, Abrikosov I A and Johansson B 2007 Redox properties of CeO_2–MO_2 (M=Ti, Zr, Hf, or Th) solid solutions from first principles calculations *Appl. Phys. Lett.* **90** 031909
[12] Hanken B E, Stanek C R, Grønbech-Jensen N and Asta M 2011 Computational study of the energetics of charge and cation mixing in $U_{1-x}Ce_xO_2$ *Phys. Rev.* B **84** 085131
[13] Scaranto J and Idriss H 2015 The effect of uranium cations on the redox properties of CeO_2 within the context of hydrogen production from water *Top. Catal.* **58** 143–8
[14] Kato M, Watanabe M, Hirooka S and Vauchy R 2023 Oxygen diffusion in the fluorite-type oxides CeO_2, ThO_2, UO_2, PuO_2, and (U, Pu)O_2 *Front. Nucl. Eng.* **1** 1081473
[15] Moser M, Pecchi M and Fend T 2019 Techno-economic assessment of solar hydrogen production by means of thermo-chemical cycles *Energies* **12** 352
[16] Idriss H 2024 A core and valence-level spectroscopy study of the enhanced reduction of CeO_2 by iron substitution—implications for the thermal water-splitting reaction *Inorganics* **12** 42
[17] Orfila M, Sanz D, Linares M, Molina R, Sanz R, Marugán J and Botas J Á 2021 H_2 production by thermochemical water splitting with reticulated porous structures of ceria-based mixed oxide materials *Int. J. Hydrog. Energy* **46** 17458–71
[18] Shelly L, Schweke D, Zalkind S, Shamir N, Barzilai S, Gouder T and Hayun S 2018 Effect of U content on the activation of H_2O on $Ce_{1-x}U_xO_{2+\delta}$ surfaces *Chem. Mater.* **30** 8650–60
[19] Prieur D, Vigier J-F, Popa K, Walter O, Dieste O, Varga Z, Beck A, Vitova T, Scheinost A C and Martin P M 2021 Charge distribution in $U_{1-x}Ce_xO_{2+y}$ nanoparticles *Inorg. Chem.* **60** 14550–6
[20] Shelly L, Schweke D, Danon A, Rosen B A and Hayun S 2023 Exploring the redox properties of $Ce_{1-x}U_xO_{2\pm\delta}$ ($x \leqslant 0.5$) oxides for energy applications *Inorg. Chem.* **62** 11456–65
[21] Al-Salik Y, Al-Shankiti I and Idriss H 2014 Core level spectroscopy of oxidized and reduced Ce*x*$U_{1-x}O_2$ materials *J. Electron Spectrosc. Relat. Phenom.* **194** 66–73
[22] Idriss H, Al-Shankiti I, Choi Y M and Al-Otaibi F M 2017 *Catalyst for Thermochemical Water Splitting* (United States of America Patents) pp 9675961
[23] Hasegawa T, Shahed S M F, Sainoo Y, Beniya A, Isomura N, Watanabe Y and Komeda T 2014 Epitaxial growth of CeO_2(111) film on Ru(0001): scanning tunneling microscopy (STM) and x-ray photoemission spectroscopy (XPS) study *J. Chem. Phys.* **140** 044711
[24] Sauerbrey M *et al* 2016 Ultrasmooth Ru(0001) films as templates for ceria nanoarchitectures *Cryst. Growth Des.* **16** 4216–24
[25] Flege J I, Höcker J, Kaemena B, Menteş T O, Sala A, Locatelli A, Gangopadhyay S, Sadowski J T, Senanayake S D and Falta J 2016 Growth and characterization of epitaxially stabilized ceria(001) nanostructures on Ru(0001) *Nanoscale* **8** 10849–56
[26] Grinter D C and Thornton G 2022 Structure and reactivity of model CeO_2 surfaces *J. Phys.: Condens. Matter* **34** 253001
[27] Zhang Y, Feng W, Yang F and Bao X 2019 Interface-controlled synthesis of CeO_2(111) and CeO_2(100) and their structural transition on Pt(111) *Chin. J. Catal.* **40** 204–13
[28] Sutter P W, Albrecht P M and Sutter E A 2010 Graphene growth on epitaxial Ru thin films on sapphire *Appl. Phys. Lett.* **97** 213101
[29] Moulder J F, Stickle W F, Sobol P E and Bomben K D 1992 *Handbook of x-ray Photoelectron Spectroscopy: A Reference Book of Standard Spectra for Identification and Interpretation of XPS Data* (Phys. Electron. Div. PerNin-Elmer Corp) p 261
[30] Allahgholi A, Flege J I, Thieß S, Drube W and Falta J 2015 Oxidation-state analysis of ceria by x-ray photoelectron spectroscopy *ChemPhysChem* **16** 1083–91
[31] Gouder T, Eloirdi R and Caciuffo R 2018 Direct observation of pure pentavalent uranium in U_2O_5 thin films by high resolution photoemission spectroscopy *Sci. Rep.* **8** 8306
[32] Tougaard S 1998 Accuracy of the non-destructive surface nanostructure quantification technique based on analysis of the XPS or AES peak shape *Surf. Interface Anal.* **26** 249–69
[33] Tougaard S 2021 Practical guide to the use of backgrounds in quantitative XPS *J Vac. Sci. Technol.* A **39** 011201

[34] Tanuma S, Powell C J and Penn D R 1994 Calculations of electron inelastic mean free paths. V. Data for 14 organic compounds over the 50–2000 eV range *Surf. Interface Anal.* **21** 165–76
[35] Kresse G and Hafner J 1993 *Ab initio* molecular dynamics for liquid metals *Phys. Rev.* B **47** 558–61
[36] Kresse G and Furthmüller J 1996 Efficient iterative schemes for *ab initio* total-energy calculations using a plane-wave basis set *Phys. Rev.* B **54** 11169–86
[37] Perdew J P, Burke K and Ernzerhof M 1996 Generalized gradient approximation made simple *Phys. Rev. Lett.* **77** 3865–8
[38] Blöchl P E 1994 Projector augmented-wave method *Phys. Rev.* B **50** 17953–79
[39] Dudarev S L, Botton G A, Savrasov S Y, Humphreys C J and Sutton A P 1998 Electron-energy-loss spectra and the structural stability of nickel oxide: an LSDA+U study *Phys. Rev.* B **57** 1505–9
[40] Yu S-W, Tobin J G, Crowhurst J C, Sharma S, Dewhurst J K, Olalde-Velasco P, Yang W L and Siekhaus W J 2011 *f*—*f* origin of the insulating state in uranium dioxide: x-ray absorption experiments and first-principles calculations *Phys. Rev.* B **83** 165102
[41] Monkhorst H J and Pack J D 1976 Special points for Brillouin-zone integrations *Phys. Rev.* B **13** 5188–92
[42] Yang Z, Luo G, Lu Z and Hermansson K 2007 Oxygen vacancy formation energy in Pd-doped ceria: a DFT+U study *J. Chem. Phys.* **127** 074704
[43] Magnéli A, Kihlborg L, Holtermann H, Sörensen J S and Sörensen N A 1951 On the cerium dioxide-uranium dioxide system and 'uranium cerium blue' *Acta Chem. Scand.* **5** 578–80
[44] Tagawa H, Fujino T, Watanabe K, Nakagawa Y and Saita K 1981 Oxidation-reduction properties of mixed oxides in the cerium-ranium-oxygen system *Bull. Chem. Soc. Japan* **54** 138–42
[45] Suresh Kumar K, Mathews T, Nawada H P and Bhat N P 2004 Oxidation behaviour of uranium in the internally gelated urania–ceria solid solutions—XRD and XPS studies *J. Nucl. Mater.* **324** 177–82
[46] El Jamal G, Gouder T, Eloirdi R, Idriss H and Jonsson M 2023 Study of water interaction with UO_2, U_2O_5, and UO_3 : tracking the unexpected reduction of uranium cations and characterization of surface-bound hydroxyls *J. Phys. Chem.* C **127** 14222–31
[47] Grau-Crespo R, De Leeuw N H, Hamad S and Waghmare U V 2011 Phase separation and surface segregation in ceria–zirconia solid solutions *Proc. R. Soc. Math. Phys. Eng. Sci.* **467** 1925–38
[48] Arts I, Saniz R, Baldinozzi G, Leinders G, Verwerft M and Lamoen D 2024 Ab initio study of the adsorption of O, O_2, H_2O and H_2O_2 on UO_2 surfaces using DFT+U and non-collinear magnetism *J. Nucl. Mater.* **599** 155249
[49] Tao F, Grass M E, Zhang Y, Butcher D R, Renzas J R, Liu Z, Chung J Y, Mun B S, Salmeron M and Somorjai G A 2008 Reaction-driven restructuring of Rh-Pd and Pt-Pd core-shell nanoparticles *Science* **322** 932–4